RESEARCH ARTICLE

EcoMat
FUNCTIONAL MATERIALS FOR GREEN ENERGY AND ENVIRONMENT

WILEY

Efficient and spectrally stable pure blue light-emitting diodes enabled by phosphonate passivated CsPbBr₃ nanoplatelets with conjugated polyelectrolyte-based energy transfer layer

Jinu Park[1] | Hyunjin Cho[2] | Joonyun Kim[1] | Yu-Ching Huang[3] | Nakyung Kim[1] | Seoyeon Park[1] | Yunna Kim[1] | Sukki Lee[1] | Jiyoung Kwon[1] | Doh C. Lee[2] | Byungha Shin[1]

[1]Department of Materials Science and Engineering, Korea Advanced Institute of Science and Technology (KAIST), Daejeon, Republic of Korea

[2]Department of Chemical and Biomolecular Engineering, Korea Advanced Institute of Science and Technology (KAIST), Daejeon, Republic of Korea

[3]Department of Materials Engineering, Ming Chi University of Technology, New Taipei City, Taiwan

Correspondence

Doh C. Lee, Department of Chemical and Biomolecular Engineering, Korea Advanced Institute of Science and Technology (KAIST), Daejeon 34141, Republic of Korea.
Email: dclee@kaist.edu

Byungha Shin, Department of Materials Science and Engineering, Korea Advanced Institute of Science and Technology (KAIST), Daejeon 34141, Republic of Korea.
Email: byungha@kaist.ac.kr

Abstract

Lead halide perovskites exhibit a very wide color gamut due to their extremely narrow emission spectra, typically characterized by a full-width at half-maximum (FWHM) of less than 20 nm. Significant advancements have been made in developing highly efficient and stable green, red, and near-infrared perovskite light-emitting diodes (PeLEDs). However, achieving efficient and stable pure blue-emitting PeLEDs remains a significant challenge. In this work, we successfully synthesized monoanionic octyl-phosphonate capped CsPbBr₃ nanoplatelets (OPA-NPLs) using a combination of octyl-phosphonic acid and oleylamine at room temperature, diverging from common approaches that necessitate complex high-temperature methods, such as hot injection, to accommodate short-chain ligands. The OPA-NPLs exhibit pure blue photoluminescence at 462 nm with a FWHM of 14 nm. Compared with CsPbBr₃ nanoplatelets synthesized using oleic acid, OPA-NPLs demonstrate significantly improved thermal stability and higher photoluminescence quantum yield (PLQY) of 90%. Additionally, we introduced Poly[(9,9-bis(3′-((N,N-dimethyl)-N-ethylammonium)-propyl)-2,7-fluorene)-alt-2,7-(9,9-dioctylfluorene)]dibromide (PFN-Br), a conjugated polyelectrolyte material, as a hole transport layer. This facilitated energy transfer between PFN-Br and the CsPbBr₃ nanoplatelets. The resulting device demonstrated an electroluminescence peak at 462 nm, an extremely narrow FWHM of 14 nm, and a maximum external quantum efficiency (EQE) of 4%. Notably, the device maintained pure blue

emission without spectral peak shift even during degradation caused by excess joule heating.

1 | INTRODUCTION

Lead halide perovskites have a wide color gamut thanks to their extremely narrow emission spectrum—typically their full-width at half-maximum (FWHM) is less than 20 nm.[1] Besides, by controlling the halogen composition and/or using the quantum confinement effect via crystal size control, it becomes feasible to manifest a spectrum encompassing not just all visible light colors but also extending into infrared and ultraviolet. Due to its superb optical properties, it is gaining popularity as a light-emitting material for next-generation displays. Perovskite light-emitting diodes (PeLEDs) have achieved remarkable progress in a short period, from an initial external quantum efficiency (EQE) of 0.1% reported in 2014[2] to achieving near-unity photoluminescence quantum yield (PLQY) and EQEs of over 20%.[3–7] In particular, red and green-emitting PeLEDs have achieved high EQEs of 25.8%[8] and 25.6%,[9] respectively. However, the development of blue PeLEDs is relatively slow,[5,10] and there is a significant challenge in meeting the display industry's requirement for pure blue emission at 467 nm (CIE $x = 0.131$, $y = 0.046$), a criterion stipulated by the Rec.2100 standard.

Several strategies have been employed to produce blue-emitting PeLEDs: (1) using a mixed halogen composition of bromide and chloride to widen the perovskite band gap, (2) forming intrinsically low-dimensional perovskites with intercalated spacers/ligands such as Ruddlesden–Popper phase, or (3) forming colloidal perovskite nanocrystals of sufficiently small size to attain quantum confinement. However, the mixed halide approach faces challenges related to spectral stability during device operation. This instability arises from phase segregation, attributed to the low formation energy of halide vacancies and the facile migration of halide ions, particularly along grain boundaries. Consequently, this instability results in shifts and broadening of the emission spectrum.[11–14] The second strategy utilizing intrinsic low-dimensional perovskites allows to achieve blue emission with a single halide composition. However, even when preparing the precursor solution with a target stoichiometric ratio, the formation of other n phases,

particularly $n = 1$ phase, readily form. The formation of the $n = 1$ phase is naturally accompanied by the substantial consumption of spacers, resulting in a phase distribution that includes higher-order domains ($n > 5$).[15,16] In a low-dimensional perovskite system with mixed $<n>$ phases, charge funneling from higher bandgap phases (lower n) to those with lower bandgaps (higher n) can occur. This phenomenon leads to a red-shifted emission from the target wavelength, posing difficulties in attaining a sharp pure blue spectrum.[17–21]

Forming colloidal nanocrystals is another approach to achieve blue emission without mixed halide compositions. Colloidal synthesis allows for tight control over crystal size distribution, and notably, the nanoplatelets (NPL) provide extremely pure colors compared with quantum dots.[22–24] In the case of CsPbBr$_3$ nanoplatelets, a thickness of 2 to 4 monolayers ($n = 2$–4) enables the realization of blue emission wavelengths in the range of 450–475 nm.[25] Consequently, early research on blue emission based on perovskite NPLs concentrated on precise control of their thickness to meet the target emission wavelengths. Additionally, efforts were made to introduce extra Pb^{2+} and Br$^-$ to promote the formation of defect-less [PbBr$_6$]$^{4-}$ octahedra.[26–30] The synthesis of CsPbBr$_3$ nanoplatelets with a uniform plate thickness necessitates the use of long alkyl chain ligands such as oleic acid (OA) and oleylamine (OLA). These ligands exhibit highly dynamic binding on the surface of the perovskite nanocrystal, leading to easy detachment during washing, aging, or dilution, which poses stability issues of the nanocrystals.[31–34] Additionally, the long alkyl chains of these ligands tend to hinder efficient charge injection, resulting in lower device efficiency. Therefore, there have been efforts to transition away from long chain ligands with dynamic binding characteristics—not only to reduce surface defects and suppress non-radiative recombination but also to enhance charge injection via substituting existing long-ligands—with shorter chain alternatives such as didodecyl dimethyl ammonium bromide, phenethylammonium bromide, triphenyl (9-phenyl-9H-carbazol-3-yl) phosphonium bromide and polyethylenimine.[35–40] While this approach improves device efficiency, it results in reduced

color purity due to the broadened FWHM of the electroluminescence (EL) spectrum compared with the photoluminescence (PL) spectrum.

Replacing longer ligands with shorter ones effectively promotes diffusion of monomeric species in perovskite precursor solutions and reduces steric hindrance, thereby enhancing the crystal growth rate. The synthesis of NPLs with distinct anisotropic structures is significantly influenced by the decrease in ligand chain length, notably affecting the distribution of phases with different n phases. Consequently, achieving a uniform small thickness requires stringent control over synthesis temperature, precursor ratios, and ligand selection.[41,42] The characteristic of having such a narrow synthesis window range poses an obstacle in the fabrication of high-efficiency and high-purity PeLEDs.

In this work, we successfully synthesized monoanionic octyl-phosphonate (OPA⁻) capped CsPbBr₃ nanoplatelets (OPA-NPLs) using a combination of octyl-phosphonic acid (OPA) and OLA instead of the traditional combination of OA and OLA. These nanoplatelets, with a thickness of 3 monolayers ($n = 3$) and designed for pure blue emission, were synthesized using a modified ligand-assisted re-precipitation method at room temperature. Unlike typical approaches that require complex high-temperature methods such as hot injection to accommodate short chain ligands, we developed a room temperature synthesis method (Figure S1). This is significant because most short chain ligands are solid at room temperature, whereas OA is liquid and miscible with toluene. Previous studies often rely on OA/OLA either during synthesis or as part of post-synthesis ligand exchange. In contrast, we identified OPA as a short chain ligand that dissolves well in non-polar solvents like toluene. Our OPA-NPLs exhibit a pure blue PL at 462 nm with a FWHM of 14 nm. Compared with CsPbBr₃ nanoplatelets synthesized with OA, OPA-NPLs demonstrate significantly enhanced thermal stability and higher PLQY. Additionally, the use of OPA ligands enhance charge carrier injection and improve device performance. With the introduction of Poly[(9,9-bis(3′-((N,N-dimethyl)-N-ethylammonium)-propyl)-2,7-fluorene)-alt-2,7-(9,9-dioctylfluorene)]dibromide (PFN-Br), a conjugated polyelectrolyte (CPE) material, as a hole transport layer (HTL), from which energy transfer through Förster resonance energy transfer (FRET) to OPA-NPLs was confirmed via transient absorption (TA) analysis, we demonstrated devices exhibiting an EL peak at 462 nm, an extremely narrow FWHM of 14 nm, and a maximum EQE of 4%. Notably, the device maintained pure blue-emission without spectral peak shift through the operating bias range up to 7 V.

2 | RESULTS AND DISCUSSION

2.1 | Characterization of phosphate-passivated CsPbBr₃ NPLs

OPA-capped CsPbBr₃ nanoplatelets (OPA-NPL) were fabricated using OPA as a ligand instead of typically used OA, employing a ligand-assisted reprecipitation (LARP) synthesis method, which allows for the entire process to be conducted at room temperature. The structural and morphological properties of OPA-NPL were characterized using transmission electron microscopy (TEM) and X-ray diffraction (XRD). Figure 1A displays a TEM image of OPA-NPL. The average lateral dimension was determined to be 15.8 ± 1.9 nm. Electron diffraction patterns corresponding to the (110), (200), and (210) planes of the cubic CsPbBr₃ phase were obtained from OPA-NPLs, as shown in the inset image. The thickness of the NPL is approximately 1.84 nm, corresponding to three monolayers ($n = 3$), based on the $[PbBr_6]^{4-}$ octahedral length of 0.6 Å in the cubic structure of CsPbBr₃.[25] The XRD pattern also matches that of the cubic CsPbBr₃ structure (JPCDS 00–054-0752), exhibiting XRD peaks associated with the (110), (200), and (210) reflections (Figure 1B).

We synthesized OA-capped CsPbBr₃ nanoplatelets (OA-NPL) without phosphonic acid as a control and investigated the incorporation of phosphonic acid in the OPA-NPL using FTIR and XPS analyses (Figure S2). In the OPA-NPL sample, FTIR peaks indicative of the P=O bond (1210–1140 cm⁻¹) and P—OH bond (920–1088 cm⁻¹), which are characteristics of phosphonic acid powder, were detected. Minor peak shifts observed in the OPA-NPL were ascribed to interactions with uncoordinated Pb^{2+} ions, as discussed in the following ³¹P nuclear magnetic resonance (NMR) analysis. The XPS spectrum exhibited a phosphonate binding energy range of 133.3–134.2 eV, corroborating the presence of phosphonate entities in the OPA-NPL sample. The interaction between OPA and the perovskite was verified through ³¹P NMR analysis (Figure 1C), conducted on solutions prepared by dispersing pure OPA powder or OPA-NPL in toluene-d₈ solvent. The solution containing only OPA exhibited a pronounced resonance at 37 ppm, aligning with neutral phosphonic acid. Conversely, the OPA-NPL sample showed a resonance at 24.7 ppm. Typically, the chemical shift of a deprotonated phosphonate ligand increases with its degree of deprotonation. Hence, the observed resonance at 24.7 ppm (chemical shift: −12.3 ppm) is indicative of the monoanionic octyl-phosphonate (OPA⁻).[43] This suggests that OPA exhibits enhanced binding stability when deprotonated to form monoanionic phosphonate (OPA⁻) species, which coordinate to Lewis acidic metal sites in CsPbBr₃ NPL crystals,[44] compared with its
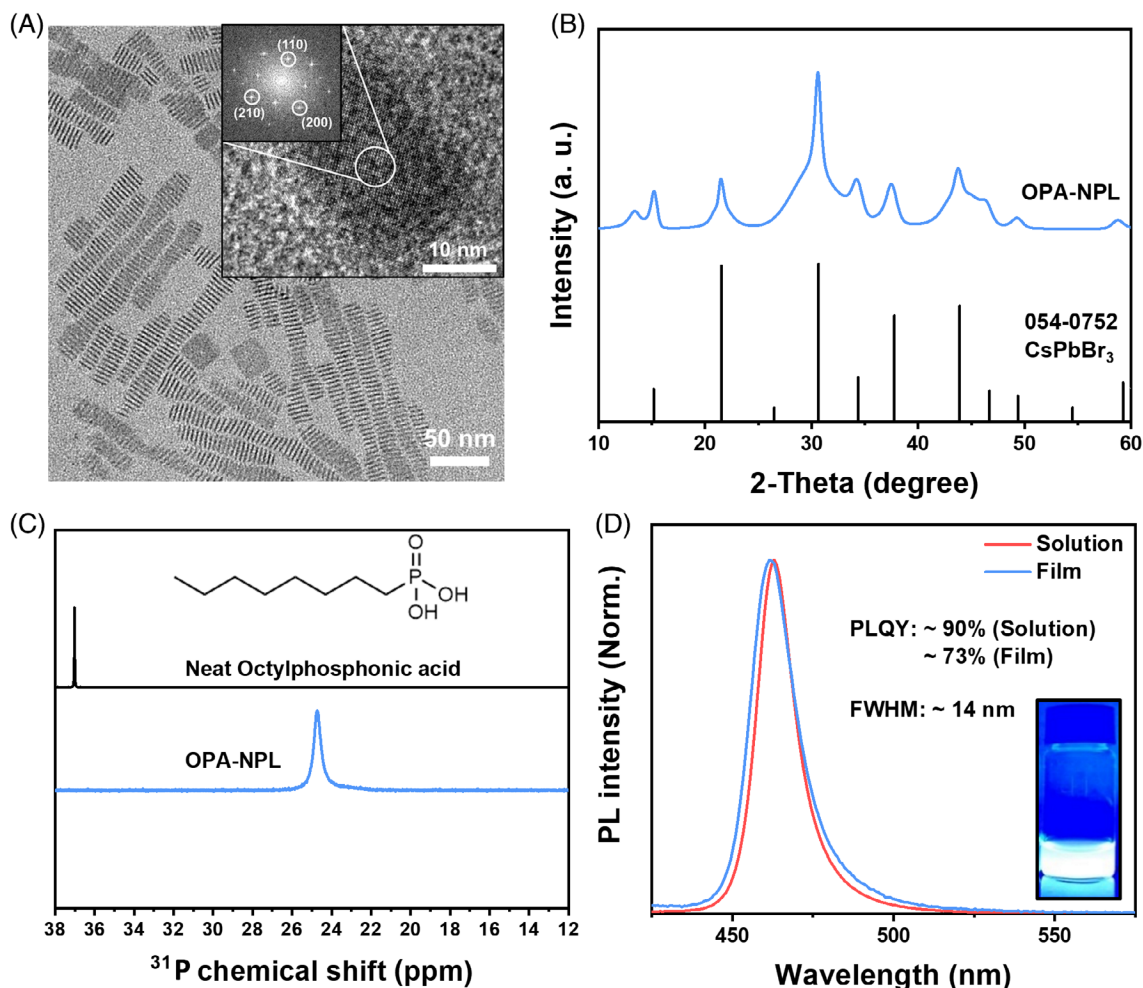
FIGURE 1 OPA-NPL characterization. (A) Transmission electron microscopy and HRTEM images (Inset: fast Fourier transform of the respective crystal, indicating the formation of cubic structure). (B) X-ray diffraction pattern. (C) Liquid-state ^{31}P nuclear magnetic resonance spectrum in toluene-d$_8$. (D) Photoluminescence spectrum (inset: digital image under UV light). FWHM, full-width at half-maximum; NPL, nanoplatelets; OPA, octyl-phosphonic acid; PLQY, photoluminescence quantum yield.

neutral bound form (OPA, chemical shift: −5.7 ppm).[43] The absence of additional resonances in the OPA-NPL solution points to the lack of unbound excess ligands, implying that the washing process during the synthesis of the nanocrystals was effective. OPA-NPL demonstrates a luminescent peak at 462 nm, accompanied by an extremely narrow emission full width at half maximum (FWHM) in both solution (∼13 nm) and film (∼14 nm) forms, and exhibits high PLQY of approximately 90% in solution and 73% in film (Figure 1D). These high PLQYs and narrow emission FWHMs imply that the synthesized nanocrystals have a uniform size distribution and minimal defects that could act as non-radiative recombination pathways. These excellent optical properties can be attributed to the chemical softness of the phosphonate group. According to the Hard and Soft Acids and Bases (HSAB) theory, soft acids prefer to bind with soft bases, while hard acids prefer to bind with hard bases.

Phosphonate, being a softer base compared with oleate, matches well with the relatively soft Pb^{2+} ions on the nanocrystal surface, effectively occupying halide vacancies and stabilizing the structure through stronger and more flexible interactions.[45] This enhanced interaction between phosphonate and Pb^{2+} improves the passivation of surface defects, leading to increased PL efficiency of the CsPbBr$_3$ NPLs.

The annealing tests were conducted on both OA-NPL and OPA-NPL to assess their temperature stability (Figure S3). In solution, after annealing at 100°C for 60 min OA-NPL preserved 70% of its initial PLQY, whereas OPA-NPL maintained over 90% PLQY. In film form, after a 10 min annealing at 70°C under ambient condition, OA-NPL retained half of its initial PLQY, while OPA-NPL sustained over 90% PLQY. The combination of OA and OLA, essential for forming size-focused nanoplatelets, exhibits highly dynamic binding behavior

on the NC surface, participating in a reversible interaction that not only leads to ligand loss during isolation and purification but also results in poor thermal stability. In contrast, phosphonic acid, which does not engage in dynamic binding behavior, forms a stable, irreversible attachment to the perovskite NC surface with a higher binding energy compared with OA.[34,46,47] Furthermore, OPA exists as a monoanionic phosphonate ligand that forms a stable network through hydrogen bonding, allowing for a more robust and stronger attachment to the $CsPbBr_3$ NPL surface.[43] Therefore, OPA-NPLs retain high PLQY even after purification and exhibit excellent thermal stability. This observation aligns with the previously presented ^{31}P NMR results, indicating that the supplied phosphonic acid binds to the $CsPbBr_3$ NPLs in a monoanionic phosphonate form.

2.2 | Effect of PFN-Br layer as energy transfer layer

In blue PeLEDs, the emissive layer often features a deep highest occupied molecular orbital (HOMO) level, which leads to slower hole injection compared with electron injection. This mismatch results in a charge imbalance, subsequently diminishing the efficiency of the device. Consequently, modifications of HTLs to enhance hole injection has been one of main strategies to improve device efficiency of blue LEDs.[48–50] We explored the application of various HTLs, commonly used for perovskite blue LEDs, including poly-TPD, PTAA, and TFB. Additionally, we also introduced PFN-Br, a type of CPE. CPEs are characterized by a polymer structure with a conjugated π-electron system along its backbone and ionic groups. When applied at the interface between two materials, the alignment of its charged groups forms a dipole moment. When the dipoles are properly aligned,

they can lower the charge injection barrier at the interface, thereby facilitating the efficiency of charge carrier injection between different materials. Additionally, it spatially separates charges, suppressing interfacial recombination.[51,52]

Except for the case with PFN-Br, the use of poly-TPD, PTAA, and TFB resulted in a parasitic emission at 432, 420, and 438 nm, respectively, distinct from the emission at 462 nm from OPA-NPL (Figure 2A). This parasitic emission occurs as some of injected electrons manage to migrate to the HTL, where they recombine with holes, leading to an expansion of the recombination zone. Additionally, excess electrons accumulated at the HTL/EML interface lead to efficiency loss through non-radiative recombination.[53] As shown in Figure 2b, the absorption spectrum of OPA-NPL overlaps with the PL spectrum of PFN-Br, the implication of which is the potential occurrence of FRET at the interface between the two layers. Compared with the PL spectra of NPL on glass (black curve in Figure 2C) and PFN-Br on glass (red curve), in the case of the NPL/PFN-Br sample (blue curve), the emission peak intensity at 430 nm from PFN-Br was quenched while the emission peak at 462 nm from the NPLs became significantly stronger, leading to a fourfold increase in the PLQY (Figure 2C). When the PFN-Br/NPL interfacial energy transfer was intentionally inhibited by inserting a 10 nm-thick LiF layer at the interface (green curve), the peak intensities of PFN-Br and OPA-NPL in the PFN-Br/LiF/NPL are similar to the PFN-Br only and the NPL-only sample, respectively, confirming that the PLQY enhancement of the PFN-Br/NPL was due to the interfacial energy transfer.

The PL spectra of poly-TPD, PTAA, and TFB also exhibit a spectral overlap with the excitonic absorption peak (455 nm) of OPA-NPL (Figure S4a). However, unlike the PFN-Br/NPL case, no drastic increase in PLQY was observed. Energy transfer between two materials can
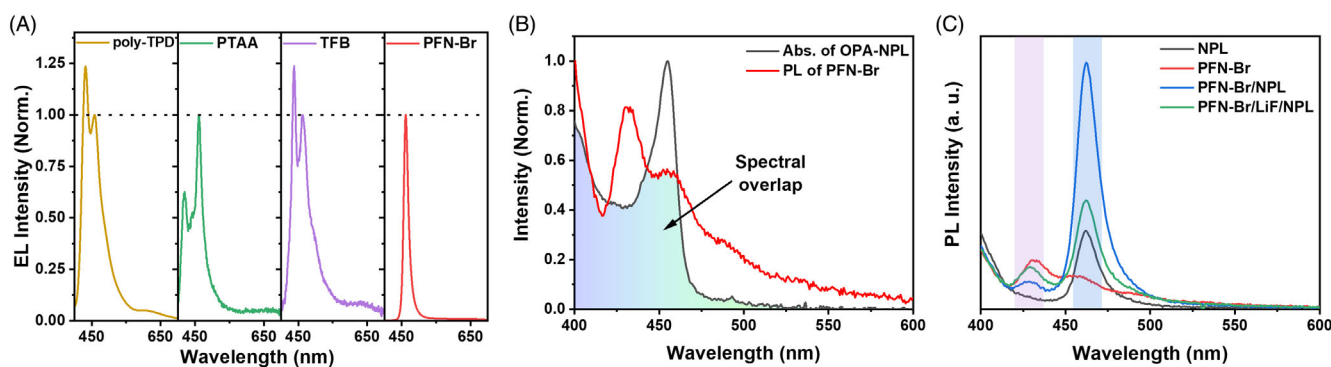

FIGURE 2 (A) Electroluminescence spectra of NPL-LEDs dependent on the hole transport layer (HTL) materials. (B) Absorption spectrum of OPA-NPL and photoluminescence (PL) spectrum of PFN-Br. (C) PL spectra of OPA-NPL with and without the PFN-Br layer and LiF treatment. NPL, nanoplatelets; OPA, octyl-phosphonic acid.

occur through FRET or Dexter energy exchange. FRET typically occurs when the distance between the donor and the acceptor is between 1 to 10 nm, whereas Dexter energy transfer is more common when the distance is less than 1 nm.[54] Given that the length of the ligands surrounding NPLs is greater than 1 nm, energy transfer between PFN-Br and NPL is more likely to occur via FRET. The probability of energy transfer via FRET depends on the degree of an overlap between the donor's emission spectrum and the acceptor's absorption spectrum, the orientation of transition dipoles, and the separation between the donor and the acceptor.[55] Therefore, due to these complex mechanisms, it is challenging to definitively conclude why efficient energy transfer between poly-TPD, PTAA, TFB, and NPL does not occur. The PL spectra of OPA-NPL coupled with poly-TPD, PTAA, or TFB film revealed that the PLQYs of the 462 nm peak, characteristic emission from OPA-NPL, were similar to that of the NPL-only sample (Figure S4b).

The enhancement factors of the PLQY for OPA-NPL deposited on poly-TPD, PTAA, TFB are 1.04, 1.02, and 0.98, respectively, while it is 3.94 for OPA-NPL on PFN-Br (Table S1).

The exciton energy transfer between PFN-Br and OPA-NPL was investigated using TA spectroscopy. The exciton number, N, was measured to be approximately 0.05 at a power 1 mW, indicating that the measurements were conducted in the single exciton region (Data S1). The TA spectra, displayed in Figure 3A–C, illustrate how the photogenerated carrier dynamics between the PFN-Br film and the adjacent OPA-NPL film influence each other. Separate samples of PFN-Br and OPA-NPL alone exhibit distinct ground state bleaching (GSB) at 415 nm and 455 nm, respectively, at selected delay times ranging from 0.1 to 500 ps (Figure 3A,B). The bilayer sample of PFN-Br and OPA-NPL also exhibits GSB signals corresponding to the both components (Figure 3C). The peak positions of these transitions correspond to the peaks
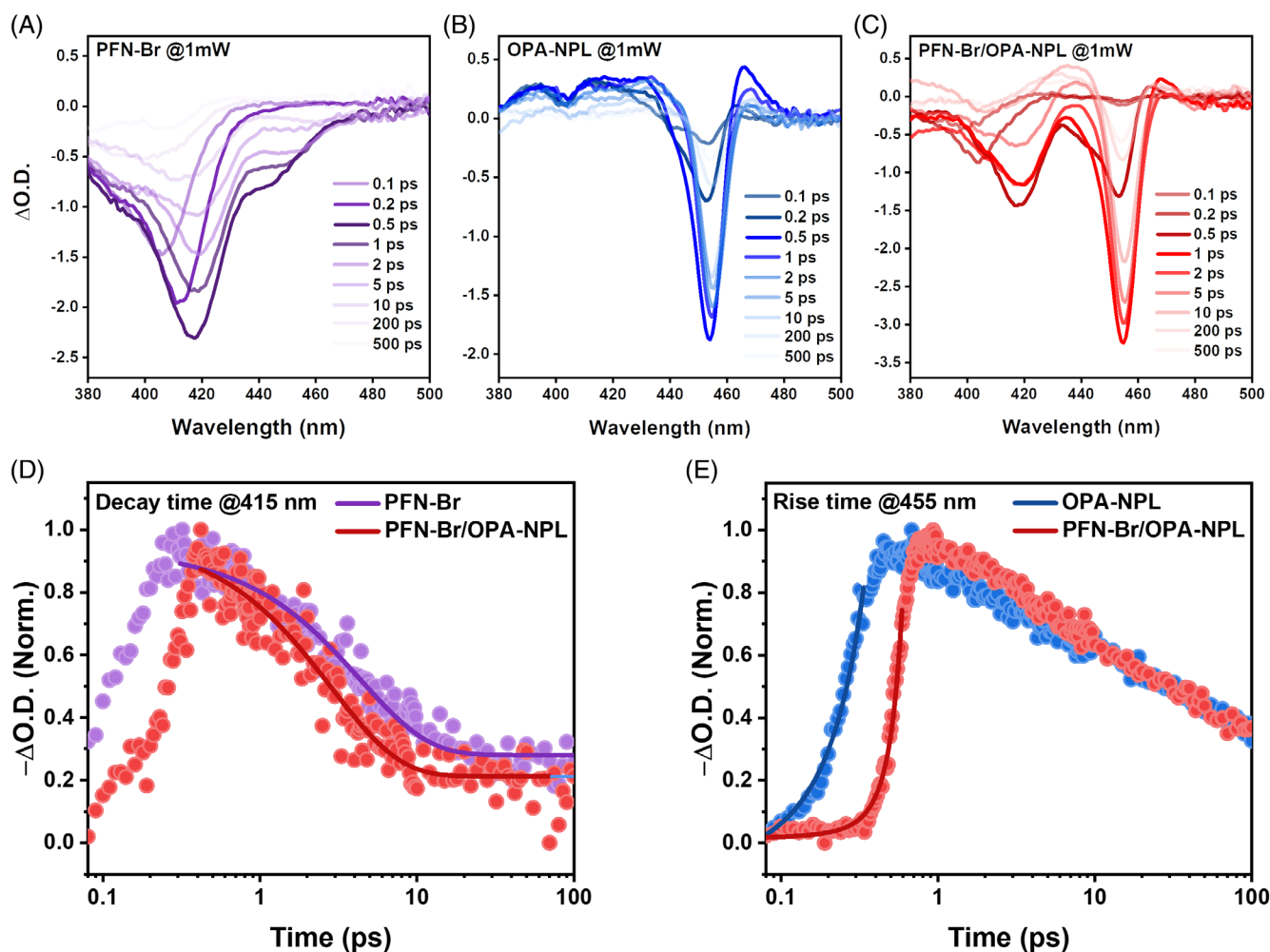
FIGURE 3 Transient absorption spectra of (A) PFN-Br, (B) OPA-NPL films and (C) PFN-Br/OPA-NPL bilayer at various delay times. Deconvolved dynamics of photobleaching features (D) PFN-Br film and PFN-Br/OPA-NPL bilayer at 415 nm and (E) OPA-NPL and PFN-Br/OPA-NPL bilayer at 455 nm. NPL, nanoplatelets; OPA, octyl-phosphonic acid.

observed in the steady-state absorption spectrum (Figure S5). In Figure 3A, the excitonic resonance at 415 nm in the PFN-Br persists even after a long excitation time of 200 ps, indicating the presence of excitons accumulated in PFN-Br up to several 100 ps of the post-pump duration.[56] Conversely, in Figure 3C, the TA spectrum of the PFN-Br/OPA-NPL sample, the exciton resonance at 415 nm corresponding to the GSB of the PFN-Br exhibits a much shorter excitation time of 10 ps, indicative of a faster decay of excitons produced in the PFN-Br. We isolated the spectra at 415 and 455 nm, corresponding to the GSB of PFN-Br and OPA-NPL, respectively, and monitored the temporal evolution of the signals in each region to visualize the ultrafast generation (rise) and decay components (Figure. 3D,E). The rise/decay curves are fitted by a multi-exponential function, $\Delta A(t) = a_1 \exp(-t/\tau_1) + a_2 \exp(-t/\tau_2) + a_3 \exp(-t/\tau_3) - c_1 \exp(-t/\tau_{rise})$, where τ_1, τ_2, and τ_3 are decay time constants, τ_{rise} the formation time constant, a_1, a_2, a_3, and c_1 amplitudes of each component. Only τ_1 and τ_{rise} are listed in Table S2 due to the complex slow decay processes such as slow energy transfer, trap-assisted recombination and auger recombination, contributing to τ_2 and τ_3.

The exciton decay time ($\tau_{1,decay}$) for the GSB of the PFN-Br film is 4.35 ps while it is much shorter, 2.86 ps, for the PFN-Br/OPA-NPL, suggesting that exciton energy transfer occurred from PFN-Br to OPA-NPL. The rise time (τ_{rise}) for the GSB of the OPA-NPL film is 0.24 ps. In contrast, the rise time of the PFN-Br/OPA-NPL exhibits a faster rise time of 0.12 ps. This reduction in rise time further supports exciton accumulation in the acceptor, and is predominantly governed by energy transfer from the donor material.[57,58] This suggests enhanced photocarrier transfer from PFN-Br to OPA-NPL, in consistent with the shortened decay time of the PFN-Br when it is coupled with the OPA-NPL layer.[59] Comparing the TRPL decay of an OPA-NPL film and PFN-Br/OPA-NPL bilayer structure (Figure S6), a slight increase in PL lifetime, from 2.89 to 3.2 ns, was observed at the 462 nm emission peak of the NPL in the bilayers. Considering the near-unity PLQY of the OPA-NPL without PFN-Br, it is inferred that PFN-Br primarily induces rapid energy transfer rather than interface passivation effects.[56,60] When a thin layer of LiF (~10 nm) was intentionally inserted at the PFN-Br/OPA-NPL interface, the decay time of PFN-Br increased back to 4.95 ps, similar to the case of the PFN-Br film alone without NPL, and the rise time of OPA-NPL increased back to 0.17 ps. The insertion of LiF restored the time scales of the exciton dynamics to those observed in the individual samples of PFN-Br only and OPA-NPL only (Figure S7). The exciton decay times and exciton formation (rise) times under each condition are summarized in Table S2.

2.3 | Device performance

EL devices were fabricated with the following device structure: ITO/PEDOT:PSS/HTL (poly-TPD, PTAA, TFB, or PFN-Br)/OPA-NPL (25 nm)/TPBi/LiF/Al (Figure 4A). Energy level diagram is presented in Figure 4B. The PFN-Br, with its relatively shallow LUMO level and deep HOMO level, helps confine the charge recombination zone within the NPL. Additionally, the conjugated π-electron system of PFN-Br, when positioned at the interface between two materials, results in the alignment of its charged groups, thereby generating dipole moments.[61,62] This arrangement lowers the charge injection barrier at the interface, enhancing efficient charge carrier injection across various materials. It also encourages the spatial separation of charges, reducing interfacial recombination. Therefore, PFN-Br in our device structure is expected to prevent parasitic emission by enhancing energy transfer between PFN-Br and OPA-NPLs. Figure 4C,D compare the J-V-L and EQE-J characteristics of devices with and without the application of OPA ligands and PFN-Br. The combination of OPA-NPL and the PFN-Br layer exhibits the lowest shunt path current as well as the highest injection current at operating biases beyond the threshold voltage for EL operation. This order of injection current is PFN-Br/OPA (due to the injection assistance of PFN-Br), OPA (due to the assistance of short ligands), and PFN/OA (with longer ligands). While combining PFN-Br with OA-NPL slightly reduces a shunt path current, the longer ligand chains of OA concurrently increase series resistance, resulting in hampered carrier injection and a subsequent reduction in luminous efficiency. Consequently, the operational performance of the devices is observed over a current density range from 0.058–10.06 mA/cm². In contrast, when applying OPA without PFN-Br, its relatively shorter chain length leads to a lower series resistance and an expanded range of luminescing in terms of current density (from 0.025–26.6 mA/cm²) compared with OA-NPL. This is linked to enhanced thermal stability from the OPA ligand application, which subsequently enhances stability against joule heating during device operation.

The J-V characteristics of OPA-NPL LEDs with varying thicknesses of PFN-Br are shown in Figure S8a. Specifically, PFN-Br concentrations of 0.1, 0.5, 1, 1.5, and 2 mg/mL correspond to thicknesses of 2.5, 4.3, 6.2, 8.8, and 11.7 nm, respectively. The maximum EQE initially rises with increasing PFN-Br thickness. This trend is attributed to improved interface passivation and energy transfer. However, as the thickness of PFN-Br increases, its insulating nature leads to decreased current density. The peak EQE is achieved at a thickness of 6.2 nm, corresponding to the PFN-Br concentration of 1 mg/mL.
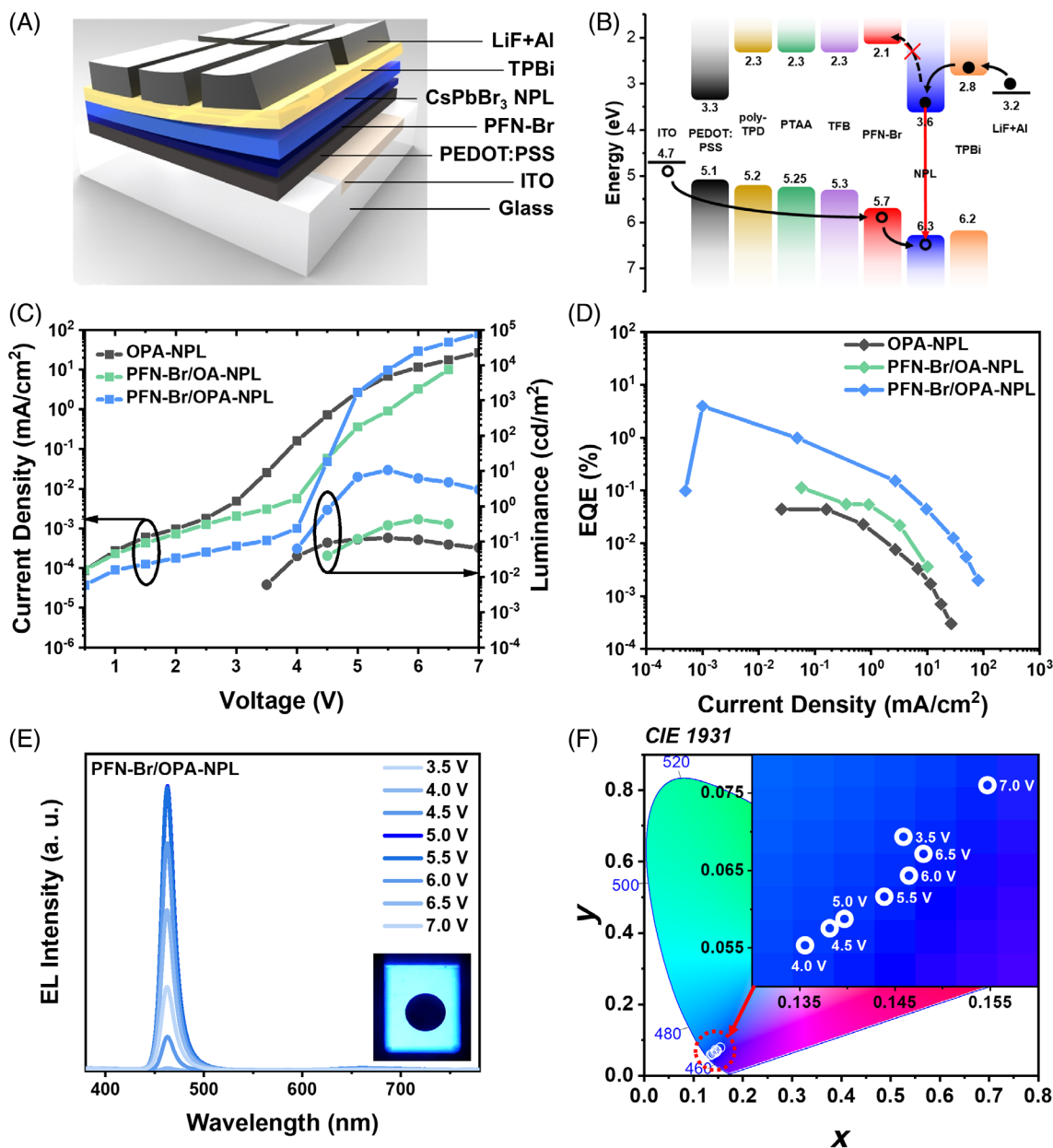
FIGURE 4   (A) Optimized device structure, (B) Flat band energy level diagram of perovskite LEDs, (C) Current Density-Voltage-Luminance (J-V-L) curves, (D) external quantum efficiency (EQE) corresponding to current density of NPL-LEDs, (E) electroluminescence (EL) spectra (Inset: digital photo of LED during operation), (F) CIE coordinates of PFN-Br/OPA-NPL device as function of voltage. NPL, nanoplatelets; OPA, octyl-phosphonic acid.

Beyond this point, a further increase in PFN-Br thickness leads to difficulties in charge injection, negatively impacting the device's performance, as shown in Figure S8b,c. Optimal PFN-Br condition at 1 mg/mL leads to achieve an EQE of up to 4% across a broad current density range from 0.00496–79.94 mA/cm^2 (Figure 4D), demonstrating suppressed EQE-roll off in comparison to the other configurations. The champion EQE value is much higher compared with 0.044% from OPA-NPL and 0.13% from PFN-Br/OA-NPL. As evident from the EL spectra shown in Figure 4E, the PFN-Br/OPA-NPL LED exhibits a luminescent peak at 462 nm with an extremely narrow FWHM of 14 nm and no parasitic emission. This device maintains high spectral stability, with no peak shifts or degradation in spectral shape, up until the device is thermally damaged by excessive joule heating at an applied bias of ~7 V. As shown in Figure 4F, the CIE coordinates indicate that the most pure-blue emission occurs at 4.0 V ($x = 0.136$, $y = 0.0553$), shifting to ($x = 0.155$, $y = 0.0760$) at 7 V. Throughout the device operation, the EL emission

consistently exhibits pure blue emission with minimal variation.

3 | CONCLUSION

In summary, we have developed surface-passivated CsPbBr$_3$ NPLs with high efficiency and uniformity by employing a room-temperature synthesis method that utilizes short-chain ligands of OPA. This method challenges the traditional view by successfully utilizing OPA ligands instead of OA ligands, previously considered indispensable for fabricating NPLs with uniform small *n* phases. OPA-NPLs exhibit a photoluminescent spectrum peak at 462 nm, corresponding to pure blue, with an extremely narrow FWHM of 14 nm. Additionally, OPA-NPL exhibits a high PLQY of 90% in solution and 70% in film. The introduction of OPA, compared with oleate, facilitates a softer chemical interaction wherein phosphonates effectively occupy halide vacancies by interacting with Pb^{2+} ions, thereby efficiently passivating the NPLs. OPA-capped NPLs greatly improve thermal stability and carrier injection in blue-emitting CsPbBr$_3$ NPLs. Furthermore, we demonstrated that PFN-Br, a CPE material, facilitates energy transfer to OPA-NPLs and enhances device efficiency when inserted at the interface between the HTL and NPLs. Using highly uniform OPA-NPLs and PFN-Br films, we demonstrated an optimized device with an efficiency of 4% for high-efficiency pure blue PeLEDs. The device's EL spectrum peak at 462 nm with a very narrow 14 nm FWHM maintained spectral stability up until the device is thermally damaged by excessive Joule heating. Our research underscores the importance of surface modification and interface control in NPLs, paving a new path for realizing high-efficiency pure blue PeLEDs.

4 | EXPERIMENTAL SECTION

4.1 | Materials

Cesium bromide (CsBr, 99.999%), lead bromide (PbBr$_2$, 99.999%), dimethyl sulfoxide (DMSO, 99.9%), hydrobromic acid (HBr, 48%), OA (90%), OLA (70%), octylphosphonic acid (OPA, 97%), toluene (99.9%), 1-hexanol (99%), ethyl acetate (EA, 99.9%), acetonitrile (ACN, 99.9%) and methanol (MeOH, 99.8%) were purchased from Sigma-Aldrich. Acetone (ACT), isopropyl alcohol (IPA) were purchased from DUCKSAN. Poly(3,4-ethylenedioxythiophene)-poly(styrenesulfonate) (PEDOT:PSS,

Al 4083, Heraeus), Poly[(9,9-bis(3′-((N,N-dimethyl)-N-ethylammonium)-propyl)-2,7-fluorene)-alt-2,7-(9,9-dioctylfluorene)]dibromide (PFN-Br, 1-Material), Poly[N,N′-bis(4-butylphenyl)-N,N′-bisphenylbenzidine] (poly-TPD, EMNI), Poly[bis(4-phenyl)(2,4,6-trimethylphenyl)amine] (PTAA, EMNI), Poly[(9,9-dioctylfluorenyl-2,7-diyl)-co-(4,4′-(N-(4-sec-butylphenyl)diphenylamine)] (TFB, EMNI), 1,3,5-Tris(1-phenyl-1Hbenzimidazol-2-yl)benzene (TPBi, Lumtec), lithium fluoride (LiF), aluminum (Al). All materials were used without any further processing.

4.2 | Preparation of the precursor solution

The CsBr precursor was prepared by dissolving CsBr in HBr to make a 1 M solution, and the 0.5 M PbBr$_2$ precursor was prepared by dissolving PbBr$_2$ in DMSO. OPA-toluene was prepared by dissolving OPA in toluene to make a 0.15 M solution. All solutions were prepared at room temperature by vortexing overnight.

4.3 | Synthesis of 3 ML CsPbBr$_3$ NPLs

Under vigorous stirring, 0.5 mL of OA and OLA were added to 5 mL of toluene (for OA-NPLs), followed by 100 uL of CsBr and PbBr$_2$ precursor solutions. For OPA-NPLs, 0.5 mL of OLA was added to 5 mL of OPA-toluene, and the same amount of CsBr and PbBr$_2$ precursor solutions were injected. A 0.5 mL of 1-hexanol was swiftly injected 10 s after adding all precursors, and the mixture was stirred for 10 min. After the reaction, the crude solution was centrifuged for 5 min at 6000 rpm. The supernatant was mixed with ACT and centrifuged for 5 min at 11000 rpm for the first purification. In order to second purification, the supernatant was discarded, and the precipitate was re-dispersed in toluene and mixed with EA in a 2:1 ratio relative to toluene. The third purification was done using the same procedure, mixing with ACN. Finally, precipitates were resuspended in 1 mL of toluene, the agglomerated particles were removed by centrifugation for 3 min at 4000 rpm, and the supernatant was filtered through a 0.5 um syringe filter. All procedures were conducted at room temperature. The 462 nm emissive 3 ML OPA-NPLs had an average concentration of around 10 mg/mL. We analyzed the stacked orientation of NPLs in different dispersion solvents (toluene or hexane) using GIWAXS analysis (Figure S9). The results showed that the (100), (101), and (102) planes of NPLs dispersed in

toluene were more orderly assembled in the in-plane direction on the substrate.

4.4 | Device fabrication

The ITO-patterned glass substrates were sequentially cleaned by ultrasonication in deionized water, acetone, and isopropyl alcohol and then treated with UV-Ozone for 25 min. The PEDOT:PSS aqueous solution was spin-coated (4000 rpm, 50s) onto the ITO substrates and annealed at 200°C for 20 min in ambient air. After transferring the samples into a nitrogen-filled glove box, the PFN-Br (various concentrations, in MeOH) precursor solution was spin-coated onto the PEDOT:PSS film at 5000 rpm for 20 s. The NPL solution was spin-coated onto the PFN-Br layer at 2000 rpm for 50 s. TPBi (50 nm), LiF (1 nm), and Al (100 nm) layers were sequentially deposited using thermal evaporation under high vacuum conditions (3×10^{-6} Torr). The effective area of the PeLEDs was determined by the intersection of the ITO and Al electrodes, which measured 5 mm^2.

4.5 | Characterization

The XRD pattern of the OPA-NPL film was analyzed using a SmartLab (RIGAKU) system equipped with Cu Kα radiation ($\lambda = 0.154$ nm) at the KAIST Analysis Center for Research Advancement (KARA). The X-ray photoelectron spectroscopy (XPS) analyses were conducted at KARA using Sigma Probe (Thermo VG Scientific) equipment with a He I ultraviolet radiation source (21.22 eV). The steady-state PL of samples was measured using an F-7000 FL spectrophotometer (HITACHI) with an excitation wavelength of 370 nm. The absorption spectra were measured using a UV-1800 UV–VIS spectrophotometer (SHIMADZU). The PLQY was obtained with a C13534-11 Quantaurus-QY Plus UV–NIR absolute PL quantum yield spectrometer (HAMAMATSU). The time-resolved photoluminescence (TRPL) decay curves were measured using a Fluorolog3 equipped with TCSPC (HORIBA SCIENTIFIC), with an excitation wavelength of 374 nm. The J-V-L characteristics and the EL spectra of the PeLEDs were measured using a system that couples a Keithley 2635A source meter with a CS-2000 spectroradiometer. The TEM samples were prepared by drop casting 10 uL of diluted NPL solution in toluene on a TEM Grid (300 mesh Cu) and imaged employing a JEM-2100F (JEOL) operated at 200 kV. The Fourier transform infrared (FTIR) spectra were measured at KARA using a Nicolet iS50 instrument (Thermo Fisher Scientific). The ^{31}P NMR spectra of the neat OPA and OPA-NPL samples were recorded using an Avance Neo 600 spectrometer (Bruker) at KARA. Before the measurements, the samples were dispersed in toluene-d$_8$ (99 atom% D, Sigma-Aldrich). The TA measurements were conducted using a pulsed regeneratively amplified Yb:KGW laser system (Pharos, Light Conversion). The laser emitted pulses with a wavelength of 1028 nm, a pulse duration of 196 fs, and a repetition rate of 200 kHz. The fundamental beam served as the seed for an optical parametric amplifier (Orpheus, Light Conversion), which generated the pump beam using a second harmonic module. The pump beam had a wavelength of 360 nm, a beam radius of approximately 130 μm. A portion of the fundamental beam (1028 nm) was utilized as the probe beam. It passed through a delay line and was focused onto a sapphire plate to generate white-light continuum using a TA spectrometer (Harpia, Light Conversion). Subsequently, this probe beam (with a beam radius of 105 μm) was focused onto the sample, overlapping with the pump beam area. The detector (Kymera 193i, Andor) was used to collect the probe beam that passed through the sample. Grazing incidence wide-angle X-ray Scattering (GIWAXS) measurements were conducted at beamline 23A1 (BL 23A1) of National Synchrotron Radiation Research Center (NSRRC) in Taiwan. The experiments utilized a monochromatic X-ray beam with a photon energy of 10 keV, corresponding to a wavelength of 1.2398 Å. The incident angle of 0.2° was used to ensure full penetration of the thin film. A flat-panel detector (model C10158DK, 2352 pixels) was used to capture the wide-angle scattering signals, with a sample-to-detector distance of 18.65 cm and a collection time of 60 s per measurement. Scattering intensities were processed using standard calibration and background subtraction procedures, and are presented as a function of scattering vector, Q, where $Q = 4\pi(\sin\theta)/\lambda$, with θ representing half the total scattering angle and λ representing the X-ray wavelength. The out-of-plane (op) GIWAXS profiles were extracted from the 2D GIWAXS patterns along a direction perpendicular to the substrate and film surface. The in-plane (ip) GIWAXS profiles were similarly extracted from the 2D GIWAXS patterns along the direction parallel to the substrate.

AUTHOR CONTRIBUTIONS
Jinu Park, Joonyun Kim, and Byungha Shin conceptualized the project. Jinu Park and Joonyun Kim designed the experiments. Jinu Park collected and analyzed the data, and wrote the original draft with input from all authors. Hyunjin Cho conducted the TAS analysis, while Yu-Ching Huang performed the GIWAXS analysis. Nakyung Kim, Seoyeon Park, Yunna Kim, Sukki Lee, and Jiyoung Kwon carried out the optical characterizations. Doh C. Lee and Byungha Shin supervised

the project and provided guidance. All authors discussed the results and contributed to the manuscript revisions.

CONFLICT OF INTEREST STATEMENT
The authors declare no conflicts of interest.

ORCID
Jinu Park https://orcid.org/0000-0001-7307-8456
Byungha Shin https://orcid.org/0000-0001-6845-0305

REFERENCES
1. Kim Y-H, Cho H, Lee T-W. Metal halide perovskite light emitters. *Proc National Acad Sci.* 2016;113(42):11694-11702. doi:10.1073/pnas.1607471113
2. Tan Z-K, Moghaddam RS, Lai ML, et al. Bright light-emitting diodes based on organometal halide perovskite. *Nat Nanotechnol.* 2014;9(9):687-692. doi:10.1038/nnano.2014.149
3. Cao Y, Wang N, Tian H, et al. Perovskite light-emitting diodes based on spontaneously formed submicrometre-scale structures. *Nature.* 2018;562(7726):249-253. doi:10.1038/s41586-018-0576-2
4. Zhao B, Bai S, Kim V, et al. High-efficiency perovskite–polymer bulk heterostructure light-emitting diodes. *Nat Photonics.* 2018;12(12):783-789. doi:10.1038/s41566-018-0283-4
5. Dong Y, Wang Y-K, Yuan F, et al. Bipolar-shell resurfacing for blue LEDs based on strongly confined perovskite quantum dots. *Nat Nanotechnol.* 2020;15(8):668-674. doi:10.1038/s41565-020-0714-5
6. Kim Y-H, Kim S, Kakekhani A, et al. Comprehensive defect suppression in perovskite nanocrystals for high-efficiency light-emitting diodes. *Nat Photonics.* 2021;15(2):148-155. doi:10.1038/s41566-020-00732-4
7. Chiba T, Hayashi Y, Ebe H, et al. Anion-exchange red perovskite quantum dots with ammonium iodine salts for highly efficient light-emitting devices. *Nat Photonics.* 2018;12(11):681-687. doi:10.1038/s41566-018-0260-y
8. Jiang J, Chu Z, Yin Z, et al. Red perovskite light-emitting diodes with efficiency exceeding 25% realized by co-spacer cations. *Adv Mater.* 2022;34(36):2204460. doi:10.1002/adma.202204460
9. Ma D, Lin K, Dong Y, et al. Distribution control enables efficient reduced-dimensional perovskite LEDs. *Nature.* 2021;599(7886):594-598. doi:10.1038/s41586-021-03997-z
10. Wang C, Han D, Wang J, et al. Dimension control of in situ fabricated CsPbClBr$_2$ nanocrystal films toward efficient blue light-emitting diodes. *Nat Commun.* 2020;11(1):6428. doi:10.1038/s41467-020-20163-7
11. Li G, Rivarola FWR, Davis NJLK, et al. Highly efficient perovskite nanocrystal light-emitting diodes enabled by a universal crosslinking method. *Adv Mater.* 2016;28(18):3528-3534. doi:10.1002/adma.201600064
12. Brennan MC, Draguta S, Kamat PV, Kuno M. Light-induced anion phase segregation in mixed halide perovskites. *ACS Energy Lett.* 2018;3(1):204-213. doi:10.1021/acsenergylett.7b01151
13. Motti SG, Patel JB, Oliver RDJ, Snaith HJ, Johnston MB, Herz LM. Phase segregation in mixed-halide perovskites affects charge-carrier dynamics while preserving mobility. *Nat Commun.* 2021;12(1):6955. doi:10.1038/s41467-021-26930-4
14. Lee H, Boonmongkolras P, Jun S, et al. In situ observation of photoinduced halide segregation in mixed halide perovskite. *ACS Appl Energy Mater.* 2023;6(3):1565-1574. doi:10.1021/acsaem.2c03438
15. Xing J, Zhao Y, Askerka M, et al. Color-stable highly luminescent sky-blue perovskite light-emitting diodes. *Nat Commun.* 2018;9(1):3541. doi:10.1038/s41467-018-05909-8
16. Yang X, Zhang X, Deng J, et al. Efficient green light-emitting diodes based on quasi-two-dimensional composition and phase engineered perovskite with surface passivation. *Nat Commun.* 2018;9(1):570. doi:10.1038/s41467-018-02978-7
17. Yang X, Chu Z, Meng J, et al. Effects of organic cations on the structure and performance of quasi-two-dimensional perovskite-based light-emitting diodes. *J Phys Chem Lett.* 2019;10(11):2892-2897. doi:10.1021/acs.jpclett.9b00910
18. Lee SY, Nam YS, Yu JC, et al. Highly efficient flexible perovskite light-emitting diodes using the modified PEDOT:PSS hole transport layer and polymer–silver nanowire composite electrode. *ACS Appl Mater Interfaces.* 2019;11(42):39274-39282. doi:10.1021/acsami.9b10771
19. Ren Z, Yu J, Qin Z, et al. High-performance blue perovskite light-emitting diodes enabled by efficient energy transfer between coupled quasi-2D perovskite layers. *Adv Mater.* 2021;33(1):e2005570. doi:10.1002/adma.202005570
20. Huang X, Bäuerle R, Scherz F, et al. Improved performance of perovskite light-emitting diodes with a NaCl doped PEDOT:PSS hole transport layer. *J Mater Chem C.* 2021;9(12):4344-4350. doi:10.1039/D0TC06058E
21. Guo Z, Zhang Y, Wang B, et al. Promoting energy transfer via manipulation of crystallization kinetics of quasi-2D perovskites for efficient green light-emitting diodes. *Adv Mater.* 2021;33(40):e2102246. doi:10.1002/adma.202102246
22. Riedinger A, Ott FD, Mule A, et al. An intrinsic growth instability in isotropic materials leads to quasi-two-dimensional nanoplatelets. *Nat Mater.* 2017;16(7):743-748. doi:10.1038/nmat4889
23. Cho W, Kim S, Coropceanu I, et al. Direct synthesis of six-monolayer (1.9 nm) thick zinc-blende CdSe nanoplatelets emitting at 585 nm. *Chem Mater.* 2018;30(20):6957-6960. doi:10.1021/acs.chemmater.8b02489
24. Bok JCvan der Bok, Dekker DM, Peerlings MLJ, Salzmann BBV, Meijerink A. Luminescence line broadening of CdSe nanoplatelets and quantum dots for application in W-LEDs. *J Phys Chem C.* 2020;124(22):12153-12160. doi:10.1021/acs.jpcc.0c03048
25. Butkus J, Vashishtha P, Chen K, et al. The evolution of quantum confinement in CsPbBr$_3$ perovskite nanocrystals. *Chem*

Mater. 2017;29(8):3644-3652. doi:10.1021/acs.chemmater.7b00478

26. Kumar S, Jagielski J, Yakunin S, et al. Efficient blue electroluminescence using quantum-confined two-dimensional perovskites. *ACS Nano*. 2016;10(10):9720-9729. doi:10.1021/acsnano.6b05775

27. Bohn BJ, Tong Y, Gramlich M, et al. Boosting tunable blue luminescence of halide perovskite nanoplatelets through post-synthetic surface trap repair. *Nano Lett*. 2018;18(8):5231-5238. doi:10.1021/acs.nanolett.8b02190

28. Wu Y, Wei C, Li X, et al. In situ passivation of $PbBr_6^{4-}$ octahedra toward blue luminescent $CsPbBr_3$ nanoplatelets with near 100% absolute quantum yield. *ACS Energy Lett*. 2018;3(9):2030-2037. doi:10.1021/acsenergylett.8b01025

29. Yang D, Zou Y, Li P, et al. Large-scale synthesis of ultrathin cesium Lead bromide perovskite nanoplates with precisely tunable dimensions and their application in blue light-emitting diodes. *Nano Energy*. 2018;47:235-242. doi:10.1016/j.nanoen.2018.03.019

30. Hoye RLZ, Lai M-L, Anaya M, et al. Identifying and reducing interfacial losses to enhance color-pure electroluminescence in blue-emitting perovskite nanoplatelet light-emitting diodes. *ACS Energy Lett*. 2019;4(5):1181-1188. doi:10.1021/acsenergylett.9b00571

31. Roo JD, Ibáñez M, Geiregat P, et al. Highly dynamic ligand binding and light absorption coefficient of cesium lead bromide perovskite nanocrystals. *ACS Nano*. 2016;10(2):2071-2081. doi:10.1021/acsnano.5b06295

32. Zhang Y, Siegler TD, Thomas CJ, et al. A "tips and tricks" practical guide to the synthesis of metal halide perovskite nanocrystals. *Chem Mater*. 2020;32(13):5410-5423. doi:10.1021/acs.chemmater.0c01735

33. Trizio LD, Infante I, Manna L. Surface chemistry of lead halide perovskite colloidal nanocrystals. *Acc Chem Res*. 2023;56(13):1815-1825. doi:10.1021/acs.accounts.3c00174

34. Fiuza-Maneiro N, Sun K, López-Fernández I, Gómez-Graña S, Müller-Buschbaum P, Polavarapu L. Ligand chemistry of inorganic lead halide perovskite nanocrystals. *ACS Energy Lett*. 2023;8(2):1152-1191. doi:10.1021/acsenergylett.2c02363

35. Zhang C, Wan Q, Wang B, et al. Surface ligand engineering toward brightly luminescent and stable cesium Lead halide perovskite nanoplatelets for efficient blue-light-emitting diodes. *J Phys Chem C*. 2019;123(43):26161-26169. doi:10.1021/acs.jpcc.9b09034

36. Shamsi J, Kubicki D, Anaya M, et al. Stable hexylphosphonate-capped blue-emitting quantum-confined $CsPbBr_3$ nanoplatelets. *ACS Energy Lett*. 2020;5(6):1900-1907. doi:10.1021/acsenergylett.0c00935

37. Yin W, Li M, Dong W, et al. Multidentate ligand polyethylenimine enables bright color-saturated blue light-emitting diodes based on $CsPbBr_3$ nanoplatelets. *ACS Energy Lett*. 2021;6(2):477-484. doi:10.1021/acsenergylett.0c02651

38. Wang H, Ye F, Sun J, et al. Efficient $CsPbBr_3$ nanoplatelet-based blue light-emitting diodes enabled by engineered surface ligands. *ACS Energy Lett*. 2022;7(3):1137-1145. doi:10.1021/acsenergylett.1c02642

39. Liu H, Worku M, Mondal A, et al. Efficient and stable blue light emitting diodes based on $CsPbBr_3$ nanoplatelets with surface passivation by a multifunctional organic sulfate.

40. Liu H, Shonde TB, Olasupo OJ, et al. Organic semiconducting ligands passivated CsPbBr3 nanoplatelets for blue light-emitting diodes. *ACS Energy Lett*. 2023;8(10):4259-4266. doi:10.1021/acsenergylett.3c01576

41. Pan A, He B, Fan X, et al. Insight into the ligand-mediated synthesis of colloidal $CsPbBr_3$ perovskite nanocrystals: the role of organic acid; base; and cesium precursors. *ACS Nano*. 2016;10(8):7943-7954. doi:10.1021/acsnano.6b03863

42. Cho J, Jin H, Sellers DG, Watson DF, Son DH, Banerjee S. Influence of ligand shell ordering on dimensional confinement of cesium lead bromide ($CsPbBr_3$) perovskite nanoplatelets. *J Mater Chem C*. 2017;5(34):8810-8818. doi:10.1039/C7TC02194A

43. Brown AAM, Hooper TJN, Veldhuis SA, et al. Self-assembly of a robust hydrogen-bonded Octylphosphonate network on cesium lead bromide perovskite nanocrystals for light-emitting diodes. *Nanoscale*. 2019;11(25):12370-12380. doi:10.1039/C9NR02566A

44. Keukeleere KD, Coucke S, Canck ED, et al. Stabilization of colloidal Ti, Zr, and Hf oxide nanocrystals by protonated tri-n-octylphosphine oxide (TOPO) and its decomposition products. *Chem Mater*. 2017;29(23):10233-10242. doi:10.1021/acs.chemmater.7b04580

45. Nenon DP, Pressler K, Kang J, et al. Design principles for trap-free $CsPbX_3$ nanocrystals: enumerating and eliminating surface halide vacancies with softer Lewis bases. *J Am Chem Soc*. 2018;140(50):17760-17772. doi:10.1021/jacs.8b11035

46. Smock SR, Williams TJ, Brutchey RL. Quantifying the thermodynamics of ligand binding to $CsPbBr_3$ quantum dots. *Angew Chem Int Ed*. 2018;57(36):11711-11715. doi:10.1002/anie.201806916

47. Stelmakh A, Aebli M, Baumketner A, Kovalenko MV. On the mechanism of alkylammonium ligands binding to the surface of $CsPbBr_3$ nanocrystals. *Chem Mater*. 2021;33(15):5962-5973. doi:10.1021/acs.chemmater.1c01081

48. Yu Z, Jeong WH, Kang K, et al. A polymer/small-molecule binary-blend hole transport layer for enhancing charge balance in blue perovskite light emitting diodes. *J Mater Chem A*. 2022;10(26):13928-13935. doi:10.1039/D2TA01987F

49. Sun WT, He Y, Ali MU, et al. Effect of the hole transport layer on the performance of sky-blue Dion–Jacobson perovskite light-emitting diodes. *J Mater Chem C*. 2023;11(41):14207-14216. doi:10.1039/D3TC02546B

50. Li J, Zhang D, Gao Y, et al. Hole transport layer modification for highly efficient divalent ion-doped pure blue perovskite light-emitting diodes. *Adv Opt Mater*. 2023;11(1):e2201883. doi:10.1002/adom.202201883

51. Lee BR, Yu JC, Park JH, et al. Conjugated polyelectrolytes as efficient hole transport layers in perovskite light-emitting diodes. *ACS Nano*. 2018;12(6):5826-5833. doi:10.1021/acsnano.8b01715

52. Lim K-G, Ahn S, Lee T-W. Energy level alignment of dipolar interface layer in organic and hybrid perovskite solar cells. *J Mater Chem C*. 2018;6(12):2915-2924. doi:10.1039/C8TC00166A

53. Bai W, Xuan T, Zhao H, et al. Perovskite light-emitting diodes with an external quantum efficiency exceeding 30%. *Adv Mater*. 2023;35(39):e2302283. doi:10.1002/adma.202302283

Adv Energy Mater. 2023;13(33):e2201605. doi:10.1002/aenm.202201605

54. Kim J, Hong A, Hahm D, et al. Realization of highly efficient InP quantum dot light-emitting diodes through in-depth investigation of exciton-harvesting layers. *Adv Opt Mater.* 2023;11(8) e2300088. doi:10.1002/adom.202300088

55. Hoffman JB, Alam R, Kamat PV. Why surface chemistry matters for QD–QD resonance energy transfer. *ACS Energy Lett.* 2017;2(2):391-396. doi:10.1021/acsenergylett.6b00717

56. Lei L, Seyitliyev D, Stuard S, et al. Efficient energy funneling in quasi-2D perovskites: from light emission to lasing. *Adv Mater.* 2020;32(16):e1906571. doi:10.1002/adma.201906571

57. Yantara N, Bruno A, Iqbal A, et al. Designing efficient energy funneling kinetics in Ruddlesden–Popper perovskites for high-performance light-emitting diodes. *Adv Mater.* 2018;30(33): e1800818. doi:10.1002/adma.201800818

58. Yuan M, Quan LN, Comin R, et al. Perovskite energy funnels for efficient light-emitting diodes. *Nat Nanotechnol.* 2016; 11(10):872-877. doi:10.1038/nnano.2016.110

59. Kong L, Zhang X, Li Y, et al. Smoothing the energy transfer pathway in quasi-2D perovskite films using methanesulfonate leads to highly efficient light-emitting devices. *Nat Commun.* 2021;12(1):1246. doi:10.1038/s41467-021-21522-8

60. Li M, Gao Q, Liu P, et al. Amplified spontaneous emission based on 2D Ruddlesden–Popper perovskites. *Adv Funct Mater.* 2018;28(17):e1707006. doi:10.1002/adfm.201707006

61. Zhou Y, Fuentes-Hernandez C, Shim J, et al. A universal method to produce low–work function electrodes for organic electronics. *Science.* 2012;336(6079):327-332. doi:10.1126/science.1218829

62. Liu H, Huang L, Cheng X, et al. N-type self-doping of fluorinate conjugated polyelectrolytes for polymer solar cells: modulation of dipole; morphology; and conductivity. *ACS Appl Mater Interfaces.* 2017;9(1):1145-1153. doi:10.1021/acsami.6b15678

SUPPORTING INFORMATION

Additional supporting information can be found online in the Supporting Information section at the end of this article.